

Defect Engineering in Cubic Cerium Oxide Nanostructures for Catalytic Oxidation

Neil J. Lawrence,[†] Joseph R. Brewer,[†] Lu Wang,[‡] Tai-Sing Wu,[§] Jamie Wells-Kingsbury,[†] Marcella M. Ihrig,[†] Gonghua Wang,[†] Yun-Liang Soo,^{§,||} Wai-Ning Mei,^{‡,⊥} and Chin Li Cheung^{*,†,⊥}

[†]Department of Chemistry, University of Nebraska-Lincoln, Lincoln, Nebraska 68588, United States

[‡]Department of Physics, University of Nebraska at Omaha, Omaha, Nebraska 68182, United States

[§]National Tsing Hua University, Taiwan

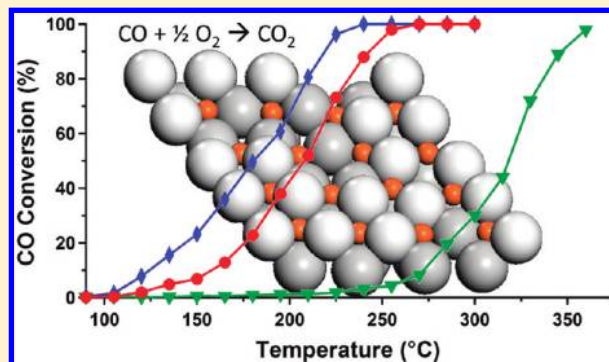
^{||}National Synchrotron Radiation Research Center, Taiwan

[⊥]Nebraska Center for Materials and Nanosciences, Lincoln, Nebraska 68588, United States

S Supporting Information

ABSTRACT: Traditional nanostructured design of cerium oxide catalysts typically focuses on their shape, size, and elemental composition. We report a different approach to enhance the catalytic activity of cerium oxide nanostructures through engineering high density of oxygen vacancy defects in these catalysts without dopants. The defect engineering was accomplished by a low pressure thermal activation process that exploits the nanosize effect of decreased oxygen storage capacity in nanostructured cerium oxides.

KEYWORDS: Heterogeneous catalysis, nanostructures, cerium oxide, oxygen vacancy defect, catalyst activation



Fluorite-structured cerium oxide (or ceria, CeO_{2-x} , $0 \leq x \leq 0.5$) has been shown to be an important material in three-way catalysis, petroleum cracking,¹ water gas shift reaction,² fuel cells,^{3,4} and synthetic organic chemistry.⁵ The relative abundance of cerium in the Earth's crust (66.5 ppm), even greater than that of copper (60 ppm), makes it an economically exciting alternative to noble metal catalysts.^{6,7} Though the role of defects in the enhancement of heterogeneous catalytic activity of ceria is well-accepted, the study of these defects and the mechanism for such enhancements is still an active area of research. Traditional engineering of catalysts typically focuses on the shape, size, and elemental composition of the catalysts. Nanostructured catalysts, which have been engineered with one or more dimensions in the nanometer-sized range, are an emerging area of research in advanced catalyst designs. Various research groups have engineered cerium oxide catalysts with features including nanodendrites,^{8,9} multifaceted surfaces,^{10–12} and/or well-defined crystal structures.^{9,13} These engineered features all have been shown to drastically improve the oxidative catalytic activity of these designer catalysts compared to those of the bulk and micrometer-sized ceria.⁵ Besides the enhanced surface-to-volume ratios in nanomaterials, the enhanced catalytic activity of these nanomaterials is often attributed to the controlled exposure specific crystalline facets with increased surface energy and thus improved reactivity.^{14,15} While it is commonly accepted that many types of defects are critical to the activity of a catalyst, few literature reports have been on the engineering of nondopant introduced oxygen vacancy

defect (OVD) sites. Additionally, the effect of OVD sites on the morphology, chemical, and electronic properties of catalysts has been under reported.

Oxygen vacancy defect sites play significant roles in the reactivity of the cerium oxide surface for the catalytic oxidation of carbon monoxide.^{16,17} This enhanced activity is often attributed to the oxygen storage capacity (OSC) of ceria, which is closely linked to the ease with which the cerium can change oxidation states. This is partially due to the similar energy of the 4f and 5d electronic states and the low potential energy barrier to electron density distribution between them.¹⁸ The valence state of the cerium is commonly discussed using the ratio $\text{Ce}^{3+}/(\text{Ce}^{3+} + \text{Ce}^{4+})$ (hereafter Ce^{3+} fraction).^{19,20} The formation of OVDs is due to a decrease in the oxygen content in the cerium oxide. Since oxygen has an oxidation state of 2– in stoichiometric CeO_2 , ceria with a high density of OVDs is expected to have an increase in its Ce^{3+} fraction in order to maintain the electrostatic.²¹ The Ce^{3+} fraction in micrometer-sized bulk cerium oxide powders, as determined by X-ray photoelectron spectroscopy (XPS), is reported to be between 0.02 and 0.25.^{19,20,22,23} Scanning tunneling microscopy (STM),^{24–26} atomic force microscopy (AFM),^{24,27–30} high-resolution transmission electron microscopy (HRTEM),³¹ Raman scattering

Received: March 3, 2011

Revised: May 20, 2011

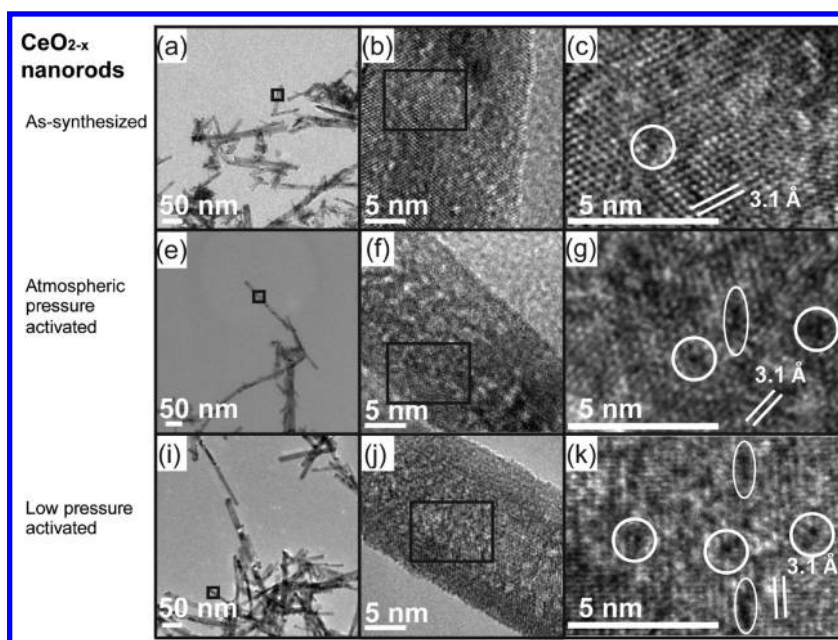


Figure 1. Transmission electron microscopy images of ceria nanorods with no postsynthesis treatment (top row), thermal activation at atmospheric pressure (middle row), and thermal activation at low pressure (0.1 Torr) (bottom row). The left column shows typical TEM images of ceria nanorods. Squares in the figures show approximate zoomed-in area of interest for adjacent figures to the right. The middle column shows HRTEM images of individual nanorods. The right column illustrates the approximate locations of some oxygen vacancy defects (OVDs). Point OVDs (circles) and linear OVDs (ovals).

spectroscopy,³² and computational studies^{16,33,34} have shown that surface, subsurface, and linear OVD sites are involved in the enhancement of the oxidation of carbon monoxide (CO) by ceria.³⁵

Here we report a conceptually different approach to improving the catalytic activity of nanosized cerium oxide (nanoceria) by increasing the OVD density without dopants. Low-pressure thermal activation was found to increase the catalytic activity of ceria nanorod and nanoparticle catalysts. The catalytic activity was evaluated by comparing light-off temperatures (T_{50}) and turn over numbers (TON). The ceria nanorods were synthesized using a modified literature procedure via hydrothermal synthesis¹² which included an extra series of harsh oxidation steps. Ceria nanorod structures were chosen as the focus for the evaluated subjects because they tended to retain a relatively high surface area even after agglomeration when compared to ceria nanoparticles. Commercially available ceria nanoparticles (NanoScale Corp., Manhattan, KS) and micrometer-sized (300-mesh) bulk ceria powder (Sigma-Aldrich, St. Louis, MO) were also evaluated as comparisons.

The as-synthesized and as-purchased ceria samples were characterized to have the cubic fluorite structure matching that of JCPDS 00-34-0394 ($Fm\bar{3}m$ CeO₂) by X-ray diffraction. Inductively coupled argon plasma optical emission spectroscopy (ICP-OES, IRIS Advantage, Thermo Jarrell Ash Corp., Franklin, MA) sampling of the ceria samples did not detect any other metal impurities. Furthermore, energy dispersive X-ray analysis (EDX, Oxford Instruments, Oxfordshire, U.K.) showed the presence of only ceria and oxygen in these samples. These results suggested that all samples consist of ceria in the fluorite structure.

High-resolution transmission electron microscopy (HRTEM) (Tecnai G² F20 S-Twin, FEI Co., Hillsboro, OR) revealed that our hydrothermally synthesized ceria was rodlike with 3.1 Å lattice fringe spacing corresponding to the (111) lattice plane spacing (Figure 1).

TEM analysis of the commercial ceria nanoparticles revealed that agglomerates of these particles have sizes between 0.1 and 1 μm. The ceria nanoparticles are highly crystalline. The size of the bulk ceria (≈ 80 μm) prevented a proper identification of the primary lattice facets by TEM. Brunauer–Emmett–Teller (BET) surface area measurements with nitrogen (ASAP 2010 Phys/Chemisorption analyzer, Micromeritics, Atlanta, GA) yielded measured surface areas of 113, 50, and 8 m²/g for ceria nanorods, ceria nanoparticles, and bulk ceria, respectively.

To generate a high density of OVDs in the nanoceria, we developed a low pressure thermal activation method which takes advantage of the large surface-to-volume ratio of nanoceria. All three types of described ceria samples were activated at 400 °C under a 30-standard-cubic-centimeter-per-minute (SCCM) gas flow composed of 20% oxygen and 80% nitrogen. Ceria samples were activated under low pressure (0.1 Torr) or atmospheric pressure to modulate the density of OVDs. A HRTEM study of these activated ceria samples indicated a high density of dark spots in the images of nanorods (Figure 1). These dark spots were well-correlated to the OVD sites identified in STM and AFM studies by other groups.^{24–32} We categorized these OVD sites either as point OVDs consisting of what appear to be single missing oxygen atoms^{24,29} or as linear OVDs composed of lines of missing oxygen atoms.²⁵ In the HRTEM images shown in panels c, f, and j of Figure 1, higher densities of point and linear OVDs can be identified in the low pressure activated when compared to those of as-synthesized or atmospheric pressure activated ceria nanorods. Dark spots, possibly point OVDs, were also observed in the HRTEM images of the ceria nanoparticles with or without activation treatment. However, we did not observe elongated dark spots on the ceria nanoparticles (see Supporting Information for images and additional information about ceria nanoparticles).

Table 1. Parameters of the Local Structure around Ce Atoms of Low Pressure Activated Ceria Nanorods, Nanoparticles, and Bulk Samples Obtained from Curve Fitting of the Ce L_{1-2} Edge EXAFS^a

CeO _{2-x} sample	neighboring atom	<i>N</i>	<i>R</i> (Å)
theoretical	O	8	2.34
	Ce	12	3.83
	O	24	4.48
nanorod	O	6.3 ± 0.1	2.294 ± 0.005
	Ce	7.4 ± 0.4	3.815 ± 0.005
	O	14.7 ± 1.2	4.515 ± 0.005
nanoparticle	O	6.5 ± 0.1	2.299 ± 0.005
	Ce	6.5 ± 0.3	3.841 ± 0.005
	O	15.5 ± 1.3	4.464 ± 0.005
bulk	O	8 ± 0.1	2.316 ± 0.005
	Ce	12 ± 0.3	3.82 ± 0.005
	O	24 ± 1.2	4.48 ± 0.005

^a *N* is the coordination number. *R* is the average interatomic distance between Ce and its neighboring atoms. Uncertainties were estimated by the double-minimum residue $2\chi^2$ method.

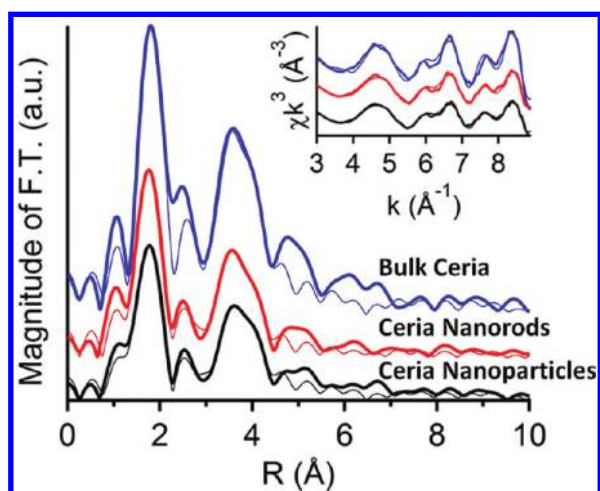


Figure 2. Fourier transforms of EXAFS spectra of (top) bulk ceria, (middle) ceria nanorods, and (bottom) ceria nanoparticles: thick lines, experimental data; thin line, curve fitted data. (Inset) *k*-space EXAFS spectra.

Extended X-ray absorption fine structure spectroscopy (EXAFS) was applied to determine the changes in the lattice atomic structures of the cerium oxide samples with different activation treatments. The local structural parameters determined by curve fitting^{36–38} of the EXAFS χ -functions extracted from the raw experimental data are listed in Table 1. The experimental EXAFS χ -functions and their Fourier transforms for the low pressure thermally activated samples are plotted with their respective curve-fitted model data in Figure 2. Compared to the theoretical bond length data of bulk ceria, the average Ce–O bond length of low pressure thermally activated nanoceria is on average 2% shorter. The coordination numbers for both the cerium and oxygen atoms in nanoceria are reduced from the theoretical values, further indicating fewer interatomic bonds than those of an ideal CeO₂ structure. Both the circumstantial evidence of shorter Ce–O bond distances and the reduction in atomic

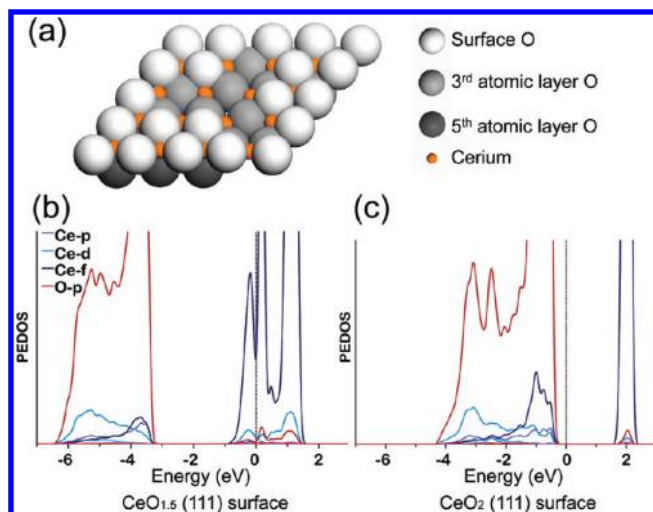


Figure 3. (a) Optimized model of (111) ceria slab corresponding to the chemical formula CeO_{1.5} showing typical surface OVDs. (b, c) Partial electronic density of states for (b) an optimized (111) CeO_{1.5} slab and (c) an optimized (111) CeO₂ slab.

coordination numbers in nanoceria suggest an increased density of OVDs in the low pressure thermally activated nanoceria.

To elucidate the bonding structures of highly defective nanoceria, we computationally modeled and optimized a (111) fluorite-structured slab model of defective ceria with a chemical formula corresponding to CeO_{1.5} (Figure 3a). The (111) surface was chosen for this study due to the very low energy nature of this surface.³⁹ The (111) surface structure of this optimized CeO_{1.5} slab model was found to contain both surface and subsurface OVDs, similar to those of STM and AFM images of defective ceria reported in the literature^{25,28,30} and observed in our HRTEM data for low pressure activated nanoceria. Significantly, the model demonstrates comparable reduction in the average Ce–O bond distance and also atomic coordination number observed in our EXAFS data (Table 1). This surface partial electronic density of states (PEDOS) was calculated from the optimized (111) CeO_{1.5} slab and compared to that of an optimized nondefective (111) CeO₂ slab (Figure 3b,c). The Ce 4*f* states are found to be partially filled for the CeO_{1.5} (111) surface. This is possibly caused by the Ce atoms adjacent to the OVDs becoming more nonbonding in nature. The defective surface is expected to be more reactive particularly near the OVD sites due to the proximity of the Fermi level to the Ce 4*f* states.

The changes in the oxidation state of the surface cerium and the relative extent of OVD density in the three different types of cerium oxide samples were qualitatively analyzed by XPS. As the fluorite structure is always retained in our samples and there is no evidence of the simple hexagonal $P\bar{3}m1$ Ce₂O₃ phase in our X-ray diffraction data, this leads us to the conclusion that the fraction of cerium in the 3+ oxidation state can be used as a parameter to compare the relative densities of OVDs in different ceria samples. The Ce³⁺ fraction for either of the purchased samples was found to be the same for the as synthesized and the atmospheric pressure activated ceria materials (Table 2). This is probably because they were likely heat-treated prior to purchase. In contrast, when the nanoceria samples were activated at 400 °C and 0.1 Torr, the analyzed XPS data suggest that the apparent Ce³⁺ fraction increased for both the ceria nanorods and the nanoparticles from 0.16 and 0.25 to 0.39 and 0.36, respectively.

Table 2. Comparison of Ce³⁺ Fractions, Turn Over Numbers, and Surface Areas of Evaluated Ceria Nanorod, Nanoparticle, and Bulk Samples^a

ceria oxide sample	Ce ³⁺ fraction		TON @200 °C μmol·g ⁻¹ ·s ⁻¹	surface area m ² /g
	before activation	after activation		
nanorod LP	0.16	0.39	2.21	113
nanorod AP	0.16	0.27	1.77	113
nanoparticle LP	0.25	0.36	0.26	50
nanoparticle AP	0.25	0.28	0.22	50
bulk LP or AP	0.25	0.25	0.01	8

^a All samples were activated at 0.1 Torr in a 100 SCCM flow of simulated air at 400 °C for 30 min. LP and AP denote ceria samples activated at 0.1 Torr and atmospheric pressure, respectively.

However, no change in Ce³⁺ fraction was detected in the bulk samples.

The presence of oxygen vacancy defects in the low pressure thermally activated ceria nanorods and nanoparticles was also indirectly implied by Raman scattering spectroscopy. Their corresponding Raman spectra were found to contain a pronounced band at 258 cm⁻¹, which was not present in those of atmospheric pressure activated ceria samples. The presence of this band has been attributed to defects with O²⁻ vacancy in ceria.⁴⁰

On the basis of the HRTEM images along with the X-ray diffraction and Raman scattering spectroscopy data, a significant increase in the density of OVDs only appears in the low pressure thermally activated nanoceria than ones activated under atmospheric pressure or those without activation. We attribute the formation of high density OVDs in these nanoceria to the low partial pressure of O₂ during the catalyst activation process and nanosize effect. During the low pressure thermal activation process the low oxygen partial pressure of the system promotes oxygen anions (O²⁻) to react and form oxygen molecules (O₂) which then desorb from the surface of the ceria nanomaterials to create OVDs. The electrostatic balance was maintained by reducing the neighboring Ce⁴⁺ to Ce³⁺, leaving behind CeO_{2-x} in a partially reduced form.⁵ Since nanoceria has a large surface-to-volume ratio, the oxygen storage capacity of each nanoceria particle is not sufficient to buffer the relatively large amount of oxygen desorbed from the surface compared to that of the micrometer sized bulk ceria. In addition, the total surface area exposed to the low pressure is expected to be a critical factor in the amount of change in the OVD density of the activated nanoceria. This is reflected by the larger change in the OVD density and Ce³⁺ fraction of the ceria nanorods which have larger surface area per gram than those of the agglomerated ceria nanoparticles (Table 2).

The effects of low pressure and atmospheric pressure activation processes on the oxidative catalytic activity of each of the three different types of ceria materials were evaluated using the bench mark test of carbon monoxide (CO) oxidation in a fixed bed reactor. The reaction $\text{CO} + \frac{1}{2}\text{O}_2 \rightarrow \text{CO}_2$ was monitored by quantifying the production of carbon dioxide (CO₂) with a gas chromatograph (GC) instrument equipped with a thermal conductivity detector. Quantified gas mixtures of CO (1.08%) and O₂ (20.1%) balanced with helium (Linweld, Inc., Lincoln, NE) was used as the reaction precursors. Typically, 0.1 g of ceria catalyst in a 30 SCCM flow of reaction gas mixture was used for each CO oxidation experiment. The surface area effect was accounted for by running catalytic reactions on a mass-adjusted sample of nanoparticles which had a surface area equal to that of the nanorods.

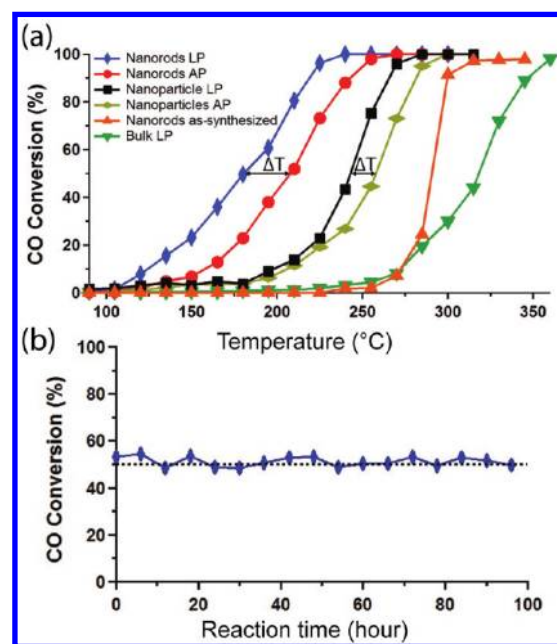


Figure 4. Catalytic activity of ceria nanorods, ceria nanoparticles, and bulk ceria toward carbon monoxide (CO) oxidation. (a) Comparison of the catalytic activity of ceria samples with no postsynthesis treatment, low pressure thermal activation, or atmospheric pressure thermal activation. The arrows indicate the change in the T_{50} (ΔT) of the same type of ceria samples activated at low pressure from ones activated at atmospheric pressure. (b) Plot of CO conversion % vs reaction time at reaction temperature of 175 °C for the low pressure thermally activated ceria nanorod catalyst.

The effect of low pressure thermal activation (0.1 Torr, LP) and atmospheric pressure thermal activation (AP) treatments on the catalytic activity of the ceria samples was revealed by comparing the T_{50} values and TON values of the differently activated samples in the CO oxidation evaluation study. As illustrated in Figure 4a and Table 2, when compared with the catalytic activity of samples treated with atmospheric pressure activation, low pressure activation treatment of the ceria nanorods decreased their T_{50} from 205 to 175 °C and increased their TON at 200 °C from 1.77 to 2.21 μmol·g⁻¹·s⁻¹. A similar trend was observed in the catalytic activity study of ceria nanoparticles. The change from low pressure activation from atmospheric pressure activation of these samples led to a decrease of the T_{50} of ceria nanoparticles from 265 to 240 °C and an increase of the corresponding TON at 200 °C from 0.22 to 0.26 μmol·g⁻¹·s⁻¹.

However, the as-synthesized ceria nanorods which had no post-synthesis treatment showed little or no activity until the reaction temperature reached 275 °C. For bulk ceria, neither low pressure nor atmospheric pressure activation treatments led to any significant changes of the T_{50} (320 °C) and TON at 200 °C ($0.01 \mu\text{mol}\cdot\text{g}^{-1}\cdot\text{s}^{-1}$) of similar bulk samples without any activation treatments.

The long-term stability and catalytic activity of the low pressure activated ceria nanorods were evaluated using the CO oxidation reaction test at their T_{50} temperature (Figure 4b). After 96 h of CO oxidation evaluation, the TON of these ceria nanorods remained about the same, suggesting that the ceria catalysts with increased OVDs are stable and are neither consumed nor deactivated during CO oxidation reaction. Further XPS study of these used catalysts indicated that their Ce^{3+} fractions remained about the same after the 96 h. reaction cycle (data not shown).

In conclusion, a nanoscale phenomenon was reported in the use of low pressure thermal annealing to increase the OVD density in cerium oxide nanoparticles and nanorods. The identification of different types of OVDs using HRTEM illustrated promising avenues in studying the structures of OVDs and their effect on the catalytic activity in ceria catalyst systems. Nanoceria thermally activated under low pressure was found to have higher TON toward CO oxidation when compared to those of nanoceria with no activation or activated at atmospheric pressure or when compared to bulk ceria. Our presented structure characterization data, catalytic activity measurements, and computation modeling results further confirm experimental observations that a high density of OVDs is a significant factor in increasing the oxidative catalytic activity of nanoceria.

■ ASSOCIATED CONTENT

S Supporting Information. Experimental details and additional spectroscopic data. This material is available free of charge via the Internet at <http://pubs.acs.org>.

■ AUTHOR INFORMATION

Corresponding Author

*E-mail: ccheung2@unl.edu.

■ ACKNOWLEDGMENT

We are grateful to David Diercks, Soumya Nag, and Nancy Bunce of the University of North Texas and Johnny Goodwin of the University of Alabama for their help with microscopy and XPS data collections. We thank the Nebraska Research Initiative, Nebraska Center for Energy Sciences Research and DOD/ARO (W911NF-10-2-0099), and NSF (EPS-1010674) for their financial support. M. M.I. was supported by a NE EPSCoR NASA fellowship.

■ REFERENCES

- (1) Bartholomew, C. H.; Farrauto, R. J. *Fundamentals of industrial catalytic processes*. 2nd ed.; Wiley: Hoboken, NJ, 2006.
- (2) Ivanova, A. S. *Kinet. Catal.* **2009**, *50* (6), 797–815.
- (3) Campos, C. L.; Roldán, C.; Aponte, M.; Ishikawa, Y.; Cabrera, C. R. *J. Electroanal. Chem.* **2005**, *581* (2), 206–215.
- (4) Murray, E. P.; Tsai, T.; Barnett, S. A. *Nature* **1999**, *400* (6745), 649–651.

(5) Trovarelli, A. *Catalysis by ceria and related materials*. 1st ed.; Imperial College Press: London, 2002.

(6) Ahrens, T. J. *Global earth physics: A handbook of physical constants*; American Geophysical Union: Washington, DC, 1995.

(7) Lide, D. *CRC Handbook of chemistry and physics*. 88th ed.; CRC Publishing Co.: Boca Raton, FL, 2007.

(8) Zhang, D.-E.; Zhang, X.-J.; Ni, X.-M.; Song, J.-M.; Zheng, H.-G. *Chem. Phys. Lett.* **2006**, *430* (4–6), 326–329.

(9) Zhong, L.-S.; Hu, J.-S.; Cao, A.-M.; Liu, Q.; Song, W.-G.; Wan, L.-J. *Chem. Mater.* **2007**, *19* (7), 1648–1655.

(10) Gonzalez-Rovira, L.; Sanchez-Amaya, J. M.; Lopez-Haro, M.; del Rio, E.; Hungria, A. B.; Midgley, P.; Calvino, J. J.; Bernal, S.; Botana, F. J. *Nano Lett* **2009**, *9* (4), 1395–1400.

(11) Pan, C.; Zhang, D.; Shi, L.; Fang, J. *Eur. J. Inorg. Chem.* **2008**, *2008* (15), 2429–2436.

(12) Zhou, K.; Yang, Z.; Yang, S. *Chem. Mater.* **2007**, *19* (6), 1215–1217.

(13) Shan, W.; Dong, X.; Ma, N.; Yao, S.; Feng, Z. *Catal. Lett.* **2009**, *131* (3), 350–355.

(14) Ozin, G. A.; Arsenault, A. C. *Nanochemistry: A chemical approach to nanomaterials*. 1st ed.; The Royal Society of Chemistry: Cambridge, U.K., 2005.

(15) Grabow, L.; Xu, Y.; Mavrikakis, M. *Phys. Chem. Chem. Phys.* **2006**, *8* (29), 3369–3374.

(16) Zhang, C. J.; Michaelides, A.; King, D. A.; Jenkins, S. J. *Phys. Rev. B* **2009**, *79* (7), 0754331–07543311.

(17) Campbell, C. T.; Peden, C. H. F. *Science* **2005**, *309* (5735), 713–714.

(18) Macedo, A.; Fernandes, S. E.; Valente, A.; Ferreira, R. A.; Carlos, L.; Rocha, J. *Molecules* **2010**, *15* (2), 747–765.

(19) Holgado, J. P.; Alvarez, R.; Munuera, G. *Appl. Surf. Sci.* **2000**, *161* (3–4), 301–315.

(20) Romeo, M.; Bak, K.; Fallah, J. E.; Normand, F. L.; Hilaire, L. *Surf. Interface Anal.* **1993**, *20* (6), 508–512.

(21) Deshpande, S.; Patil, S.; Kuchibhatla, S.; Seal, S. *Appl. Phys. Lett.* **2005**, *87* (13), 87–89.

(22) Senanayake, S. D.; Stacchiola, D.; Evans, J.; Estrella, M.; Barrio, L.; Perez, M.; Hrbek, J.; Rodriguez, J. A. *J. Catal.* **2010**, *271* (2), 392–400.

(23) Babu, S.; Thanneeru, R.; Inerbaev, T.; Day, R.; Masunov, A. E.; Schulte, A.; Seal, S. *Nanotechnology* **2009**, *20* (8), 1–5.

(24) Grinter, D. C.; Ithnin, R.; Pang, C. L.; Thornton, G. J. *Phys. Chem. C* **2010**, *114* (40), 17036–17041.

(25) Esch, F.; Fabris, S.; Zhou, L.; Montini, T.; Africh, C.; Fornasiero, P.; Comelli, G.; Rosei, R. *Science* **2005**, *309* (5735), 752–755.

(26) Hojo, H.; Mizoguchi, T.; Ohta, H.; Findlay, S. D.; Shibata, N.; Yamamoto, T.; Ikuhara, Y. *Nano Lett.* **2010**, *10* (11), 4668–4672.

(27) Croy, J. R.; Mostafa, S.; Liu, J.; Sohn, Y. H.; Cuenya, B. R. *Catal. Lett.* **2007**, *118* (1–2), 1–7.

(28) Gritschneider, S.; Reichling, M. *Nanotechnology* **2007**, *18* (4), 1–6.

(29) Lauritsen, J. V.; Reichling, M. *J. Phys.: Condens. Matter* **2010**, *22* (26), 1–23.

(30) Torbrugge, S.; Reichling, M.; Ishiyama, A.; Morita, S.; Custance, O. *Phys. Rev. Lett.* **2007**, *99* (5), 4.

(31) Liu, X.; Zhou, K.; Wang, L.; Wang, B.; Li, Y. *J. Am. Chem. Soc.* **2009**, *131* (9), 3140–3141.

(32) Wu, Z.; Li, M.; Howe, J.; Meyer, H. M.; Overbury, S. H. *Langmuir* **2010**, *26* (21), 16595–16606.

(33) Nolan, M.; Fearon, J. E.; Watson, G. W. *Solid State Ionics* **2006**, *177* (35–36), 3069–3074.

(34) Sayle, T. X. T.; Parker, S. C.; Catlow, C. R. A. *Surf. Sci.* **1994**, *316* (3), 329–336.

(35) Ganduglia-Pirovano, M. V.; Hofmann, A.; Sauer, J. *Surf. Sci. Rep.* **2007**, *62* (6), 219–270.

(36) Rehr, J. J.; Mustre de Leon, J.; Zabinsky, S. I.; Albers, R. C. *J. Am. Chem. Soc.* **1991**, *113* (14), 5135–5140.

(37) Soo, Y. L.; Ming, Z. H.; Huang, S. W.; Kao, Y. H.; Bhargava, R. N.; Gallagher, D. *Phys. Rev. B* **1994**, *50* (11), 7602–7606.

(38) Soo, Y. L.; Weng, S. C.; Sun, W. H.; Chang, S. L.; Lee, W. C.; Chang, Y. S.; Kwo, J.; Hong, M.; Ablett, J. M.; Kao, C. C.; Liu, D. G.; Lee, J. F. *Phys. Rev. B* **2007**, *76* (13), 132404–132407.

(39) Nolan, M.; Grigoleit, S.; Sayle, D. C.; Parker, S. C.; Watson, G. W. *Surf. Sci.* **2005**, *576* (1–3), 217–229.

(40) Nakajima, A.; Yoshihara, A.; Ishigame, M. *Phys. Rev. B* **1994**, *50* (18), 13297.